

Single neutron super-resolution imaging based on neutron capture event detection and reconstruction*

Yu-Hua Ma,^{1,2} Bin Tang,¹ Wei Yin,^{1,†} Hang Li,^{1,‡} Hong-Wen Huang,^{1,§} Hong-Li Chen,^{2,¶} Xin Yang,¹ He-Yong Huo,¹ Yong Sun,¹ Sheng Wang,¹ Bin Liu,¹ Run-Dong Li,¹ and Yang Wu¹

¹Chinese Academy of Engineering Physics, Mianyang 621000, China

²University of Science and Technology of China, Hefei 230026, China

Neutron capture event imaging, as a novel imaging technique, has the potential to substantially enhance the resolution of the existing imaging system. This study provides a measurement method for neutron capture event distribution and multiple reconstruction methods for super-resolution imaging. This technology can reduce the point spread function of the imaging system through single neutron detection and event reconstruction, thereby significantly improving the imaging resolution. In the experiment, a single neutron detection experiment was conducted using the highly practical and efficient ⁶LiF–ZnS scintillation screen, relying on the cold neutron imaging device on the research reactor. In milliseconds of exposure time, a large number of weak light clusters and their distribution inside the scintillation screen were recorded frame by frame, completing single neutron detection. In the calculation, several reconstruction algorithms were proposed. The location of the neutron capture event was calculated by the several processing methods such as noise removal, filtering, spot segmentation, contour analysis, and local positioning. The proposed algorithm achieves higher imaging resolution and faster reconstruction speed. Combining single neutron detection experiments and reconstruction calculations, single neutron super-resolution imaging was finally achieved. The results show that the resolution of the 100 μm thick ⁶LiF–ZnS scintillation screen can be improved from 125 microns to 40 microns. It indicates that the proposed single-neutron detection and calculation method is an effective technical route, which can significantly improve the imaging resolution.

Keywords: Neutron capture reaction, Super-resolution imaging, Weak light detection, Event reconstruction.

I. INTRODUCTION

Thanks to the development of neutron sources and the advances of neutron detection [1–4] technology, neutron imaging can attain exceptional spatial resolution and time resolution, rendering it extensively applicable across numerous fields [5–7]. Nowadays, advanced imaging methods and detection technologies are also emerging one after another [8–14]. Various neutron scintillation screens, scintillating fibers, CCD/CMOS, neutron imaging plates (NIP), and other key imaging devices have advanced performance [15–20]. It has become very difficult to physically modify imaging instrument and continue to improve the resolution of imaging systems. However, with the continuous development of technology, the demand for higher detection accuracy and more precise detection targets is increasing. This urgently requires neutron imaging technology to move towards higher resolution.

Usually, the neutron imaging detection system mainly consists of the neutron scintillation screen, mirror, lens group, CCD or CMOS [21–25]. The conclusions drawn from modern information optics theory indicate that in a spatially in-

variant linear system, any imaging device is equivalent to a filter in space. These devices will contribute to point diffusion and blur the image. Among them, the blurring effect of the scintillation screen is more critical [26, 27]. Inside the scintillation screen, neutrons will react with neutron converters such as ⁶LiF, and then the particle transport and fluorescence transport will occur. These transport processes contribute to a strong point spread effect in imaging [28]. The neutron scintillation screen has become the main factor restricting the imaging resolution and is a key component to improve the quality of neutron imaging [29].

Research on improving the resolution of imaging systems has been relatively mature [30]. In terms of hardware, the research covers device characteristics and various imaging methods [31–34]. In terms of computation, the research covers various image processing methods [5, 35–37]. The existing research mainly focuses on the high-resolution thin screens (50 μm ⁶LiF–ZnS, or thinner Gd₂O₃S screens [38, 39]), or doped (Gd/B) neutron-sensitive MCP [40]. In terms of experimental methods, single neutron detection and reconstruction is a novel imaging method. It can obtain high-resolution neutron images by experimental and computational methods without changing the original device, which is a very meaningful technical route.

This work explores a super-resolution imaging method based on single neutron detection and reconstruction. This method can detect single neutrons and remove blur caused by point diffusion. In experiment, a specific measurement method for neutron capture events was proposed in the experimental detection, and the cheap and widely used ⁶LiF–ZnS scintillation screen (100 μm) was used to complete the experimental measurement on the reactor. In the computation,

* This work was supported by (Grant No.12205271, No.12075217, No.U20B2011 and No.51978218), Sichuan Science and Technology Program (Grant No. 2019ZDZX0010) and the National Key R&D Program of China (Grant No.2022YFA1604002). Institutions are ranked alphabetically and all share a joint first rank with equal contribution.

† Corresponding author, yinwei-itm@163.com

‡ Corresponding author, lihang32@gmail.com

§ Corresponding author, hww@caep.cn

¶ Corresponding author, hlchen1@ustc.edu.cn

four reconstruction algorithms were proposed. The proposed method not only effectively extracts signals and distinguishes noise to further improve resolution, but also reduces computational complexity and improves reconstruction speed.

II. MATERIALS AND METHODS

A. Theory

In neutron radiography, incident neutrons react with ^6LiF in the scintillation screen and excite fluorescence on ZnS . Typically, conventional imaging is achieved by exposure to a scintillation screen. That is, the fluorescence distribution $I(t, s)$ is integrated over time:

$$I(s) = \int_{\text{Exposure-time}} I(t, s) dt \quad (1)$$

Where $I(t)$ represents the image, i.e., the light intensity distribution. s is the spatial position and t is the exposure time.

This work achieves single neutron detection by detecting the fluorescence spots generated by neutron reactions one by one. The precise position of the incident neutron is then calculated through a reconstruction algorithm. Using a dot with a precise location to replace the fluorescent Airy spot (light clusters), can reduce point diffusion and reduces blurring in imaging. Finally, a large number of light dot distributions are added together to form a higher-resolution neutron image.

Theoretically, the single neutron detection is equivalent to the time differential of photon distribution $I(t, s)dt$. If they are directly superimposed, the resulting image is equivalent to traditional imaging $\int I(t, s)dt$. If they are superimposed after reconstruction $P(I(t, s)dt)$, super-resolution imaging can be finally achieved.

$$I^{HR}(s) = \int_{\text{All-exposure-time}} P[I(t, s)dt] \quad (2)$$

Where $I^{HR}(s)$ represents the high-resolution image, and $P(\cdot)$ represents the reconstruction process.

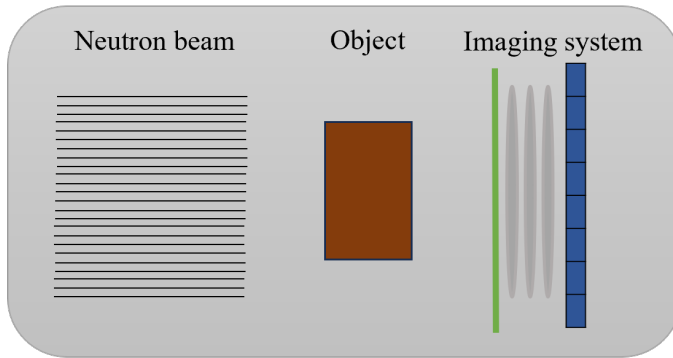
Although this method can effectively achieve super-resolution imaging, on the other hand, it also puts higher requirements on the detection technology and reconstruction algorithm. Experimentally, in order to detect a single event, the detection system needs to obtain a distinguishable weak light signal under the intrinsic noise. Computationally, every event on each frame needs to be extracted and calculated. These large number of neutron events will consume a lot of computational resources and time, and it is necessary to improve the efficiency of the algorithm. For weak light sources, the main problems faced are experimental detection and positioning calculations, among which distinguishing noise and weak light signals is the most critical aspect. Algorithms still need to improve discrimination for noise.

B. Experiment

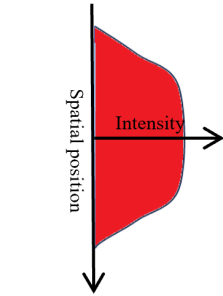
The most basic task to be accomplished in this experiment is to detect the single neutron event. In order to measure each neutron radiation capture event one by one under a continuous neutron beam, the fluorescence produced by the event and its spatial distribution need to be measured individually. The spatial distribution of fluorescence is the data basis for traditional imaging and super-resolution imaging. For one thing, the fluorescence distribution can be directly superimposed during data processing to obtain an image that is equivalent to conventional integral imaging. For another, the detection results of single neutrons can be processed to achieve super-resolution imaging.

Single neutron detection and reconstruction is the guiding ideology of the experiment, and its principle is shown in Figure 1. (I) As shown in Figure 1(a), traditional imaging detects all neutrons in one exposure time, equivalent to time integration. Each Gaussian-like spot will overlap with each other, eventually forming an image with a blurred result. (II) As shown in Figure 1(b), single neutron detection aims to detect neutrons one by one, and each individual spot distribution will be obtained. If reconstruction is not performed, all spots overlapping directly together is equivalent to the traditional imaging method. (III) As shown in Figure 1(c), single neutron super-resolution imaging aims to reconstruct the precise position of each neutron event spot by spot. By superimposing the reconstructed points with small-scale distribution (pixel-level), the spatial resolution of imaging can be significantly improved.

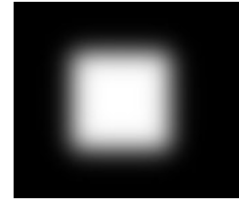
(a) Traditional imaging



Imaging system

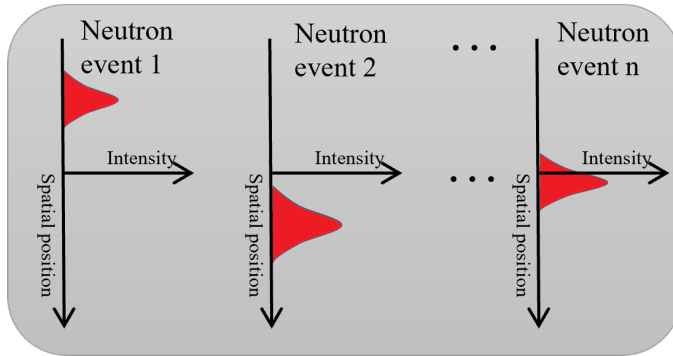


Integral imaging
(traditional imaging)

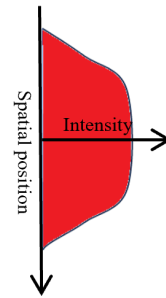


Image

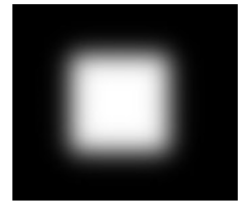
(b) Single neutron detection - no super-resolution



Single neutron detection:
Intensity distribution of fluorescence

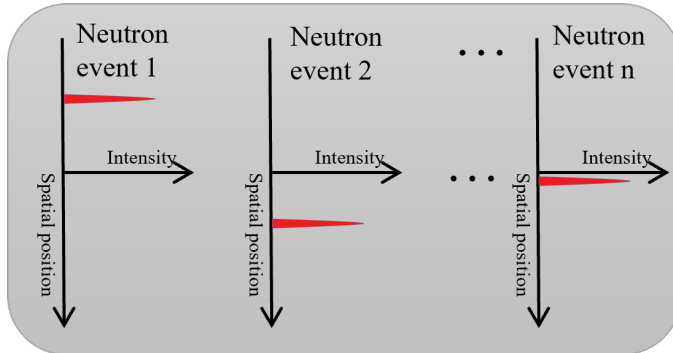


Integral imaging
by stacking events one by one

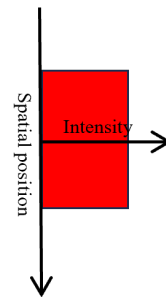


Image

(c) Single neutron detection - super-resolution imaging



Reconstruction calculation:
locating the incident position of the neutron



Super-resolution imaging



Image

Fig. 1. (Color online) Imaging method sketch: (a) Integral imaging (traditional imaging method); (b) Integral imaging based on single neutron detection; (c) Super-resolution imaging based on single neutron detection

The measurements were conducted at the Cold Neutron radiography Facility (CNRF) located at C1 beam tube of the China Mianyang Research Reactor (CMRR). The neutrons emitted from the C1 beam tube have a cold neutron spectrum with a characteristic wavelength of 0.26 nm (approximately 0.121 eV). The neutron flux can reach $3.41 \times 10^8 \text{ cm}^{-2}\text{s}^{-1}$, and the neutron flux at the sample position can reach $8 \times 10^6 \text{ cm}^{-2}\text{s}^{-1}$ [41]. A variety of collimation ratios (tube length and aperture size) are available, and the aperture size used in this work was ϕ 10 cm. The main components of the neutron imaging instrument include $^6\text{LiF-ZnS}$ scintillator screen, mirror, optical lens group, image intensifier and sCMOS camera. The Cold Neutron radiography Facility (CNRF) and its imaging system are shown in Figure 2 [42].

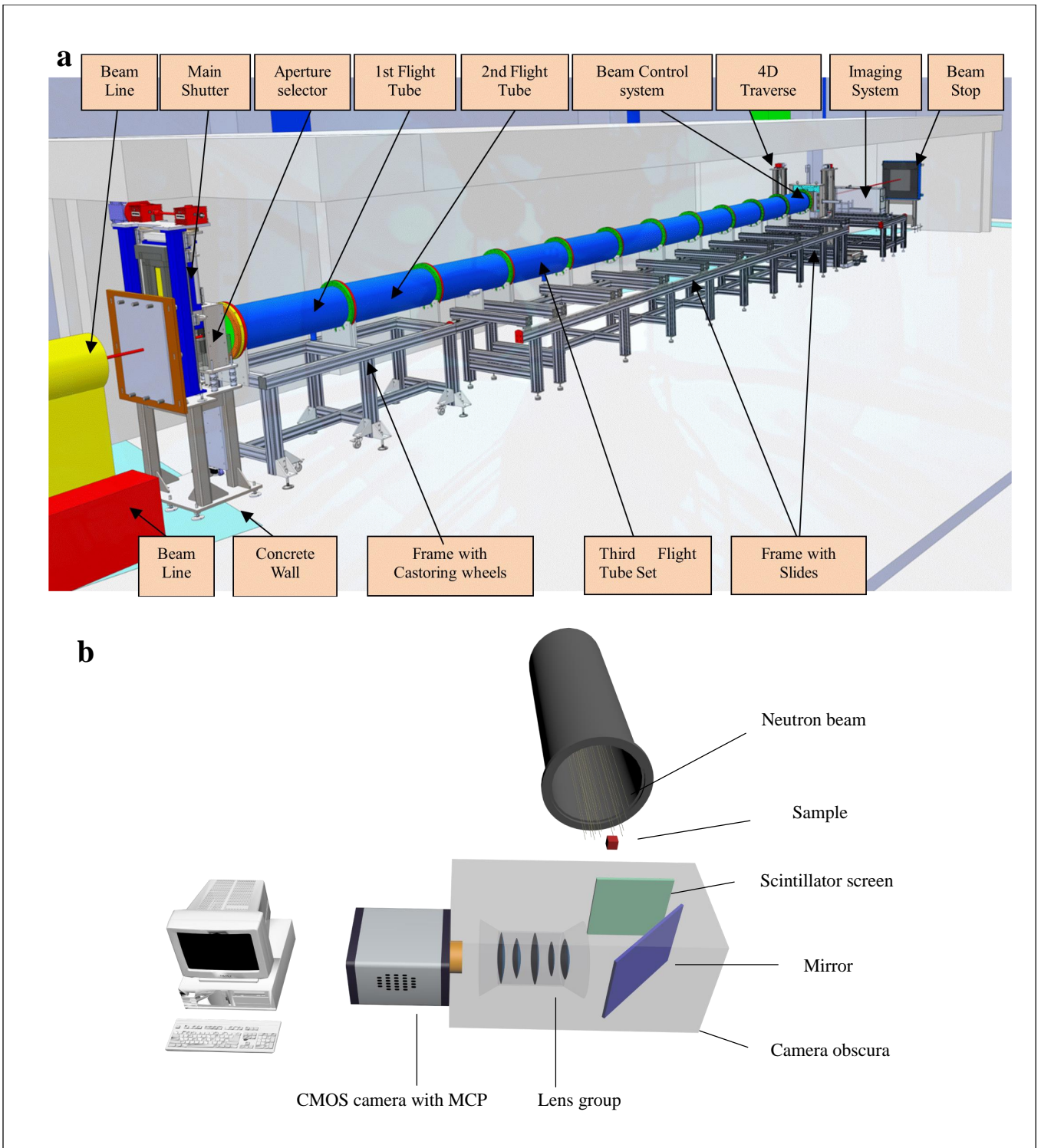


Fig. 2. (Color online) Experimental setup (a) Sketch of Cold Neutron radiography Facility; (b) Sketch of imaging system at CNRF.

The ${}^6\text{LiF}$ – ZnS scintillation screen used on CNRF is also the most widely used and cost-effective neutron scintillation screen. Aluminum with a small cross section is used as the base material of the scintillator screen, where the scintillator material with a thickness of $100\text{ }\mu\text{m}$ is coated. The scintillator screen is composed of neutron converter material ${}^6\text{LiF}$, fluorescent material $\text{ZnS}(\text{Ag})$ and binder epoxy resin in a mass ratio of 1:2:1.29. The overall density is 2.845 g/cm^3 . The typical size of ${}^6\text{LiF}$ and ZnS particles is about $1.5\text{ }\mu\text{m}$ – $5\text{ }\mu\text{m}$. The characteristic wavelength of the fluorescence spectrum is 450 nm , and the fluorescence decay time is 200 ns .

The camera used is the ANDOR iStar-sCMOS, which provides high resolution and high frame rate measurements. The camera can capture 12 bit or 16 bit images with an image array size of 2560×2560 . The camera can read out images at 50 fps frame rate with full-frame resolution and 16 bit depth. An MCP is installed in the iStar-sCMOS camera as an image intensifier, which can provide a maximum gain of 4096 times. This will facilitate the detection of weak fluorescence. MCP has a peak QE of up to 50 % and spectral coverage from 120 nm to 1100 nm . MCP uses P46 phosphor with a light decay time of 200 ns (2 ms for P43), which is the main limitation of the optical inter-frame time (300 ns). It is important that the optical resolution limit of the MCP (P46 phosphor) produced by Andor is $35\text{ }\mu\text{m}$.

When collecting images, the field of view size was adjusted to $27\text{ mm}\times 27\text{ mm}$ to cover the entire sample. The sample is a gadolinium resolution grating manufactured by the Paul Scherrer Institute. The resolution grating was placed close to the detector, to minimize the blurring caused by beam divergence. The gain of MCP was set to 2000. The detector acquires at a resolution of 2560×2560 pixels, and reads out at a interest region of 2560×1360 pixels for a higher detection frame rate. The acquisition mode was 12 bit low noise mode. To be able to detect the light spots generated by single neutrons, and to avoid the stacking of light spots as much as possible, the exposure time of the detector was set to 2 ms . After cooling the camera sensor to $0\text{ }^\circ\text{C}$, 190 thousand images were collected. After the test was finished, the beam aperture was closed, and 5 thousand dark field images were acquired for noise removal.

C. Reconstruction method

In theory, each interaction on the scintillation screen material will produce a star-shaped spot of light. In the experiment, the light spots produced by each capture reaction are recorded under very short exposure time (millisecond level). In the reconstruction, calculate the position of each light spot and assign a value to the corresponding pixel. Reconstructing each nuclear event, every frame, and eventually stacking all frames enables high-resolution imaging. Each reconstruction calculation is for a single event, making the imaging technique transform from a frame-based system to an event-based system.

In the task of single neutron super-resolution imaging, the key steps of the reconstruction algorithm are to: (i) process

image noise and extract fluorescence signals. (ii) calculate the location of neutron capture events, and reduce the point diffusion effect produced by the imaging device. Ultimately, single neutron detection combined with reconstruction enable super-resolution imaging. The schematic diagram of its principle is shown in Figure 3.

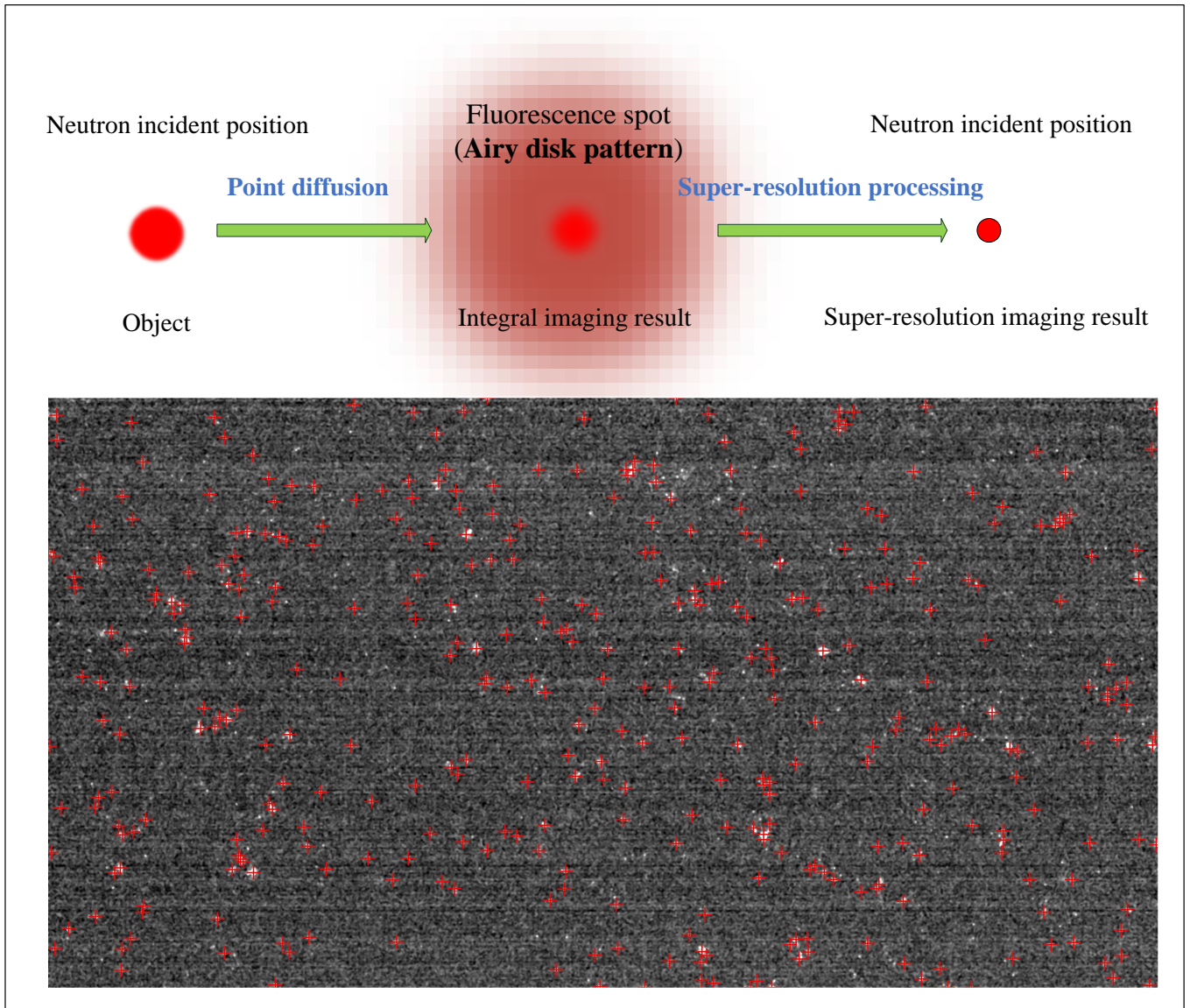


Fig. 3. (Color online) Sketch of reconstruction principle

In this work, four more advanced algorithms are proposed and reconstruction results are given. The first is an improved centroid algorithm based on the existing algorithm, and the rest are median filter centroid algorithm, median filter extremum algorithm, and Gaussian filter extremum algorithm. A sketch of the calculation process is shown in Figure 4. Compared with existing centroid algorithm (Figure 4a), these algorithms have more advantages in noise discrimination, and the calculated reconstructed images are more credible.

The calculation steps of centroid algorithm are as follows (Figure 4b): subtracting noise background, spot segmentation, contour morphology analysis and centroid calculation. In denoising, the image measured in dark field can be removed as fixed noise, leaving only some random noise. In spot segmentation, a threshold was set to eliminate random noise and low SNR light spot signals, and then each spot area was segmented and processed. In contour analysis, the position, area, perimeter and other morphological feature of contour were found and counted, and the relationship between parent and child contours was determined. In centroid calculation, the area and circumference of the contour can be taken as the condition to remove the low SNR signal and noise. Then the centroid position of the light spot is calculated to obtain a high-resolution image. Compared with the traditional method that directly calculating the spot centroid, this method can remove noise more thoroughly and can reconstruct a super-resolution image with higher credibility.

The median filter centroid algorithm is similar to the centroid algorithm (Figure 4c). The difference is that the median filter is added after subtracting the noise background, where the filter kernel covers a radius of 3 pixels. The random noise in the image is close to the signal in gray value and similar to the peak-shaped signal in shape. But the noise distribution range is smaller. The function of median filtering is to eliminate random noise similar to the signal. The advantage of median filtering is that it can remove noise with less signal loss. However, its disadvantage is that it changes the signal distribution and flattens the peak of the spot, which may change centroid position.

Median filter extremum algorithm and Gaussian filter extremum algorithm are faster reconstruction methods (Figure 4d and Figure 4e). The calculation steps of these two algorithms are: subtracting noise background, median/Gaussian filtering, spot segmentation, local extreme value calculation. Compared with the centroid algorithm, the extremum algorithm has less computation, faster reconstruction speed, and better noise reduction effect.

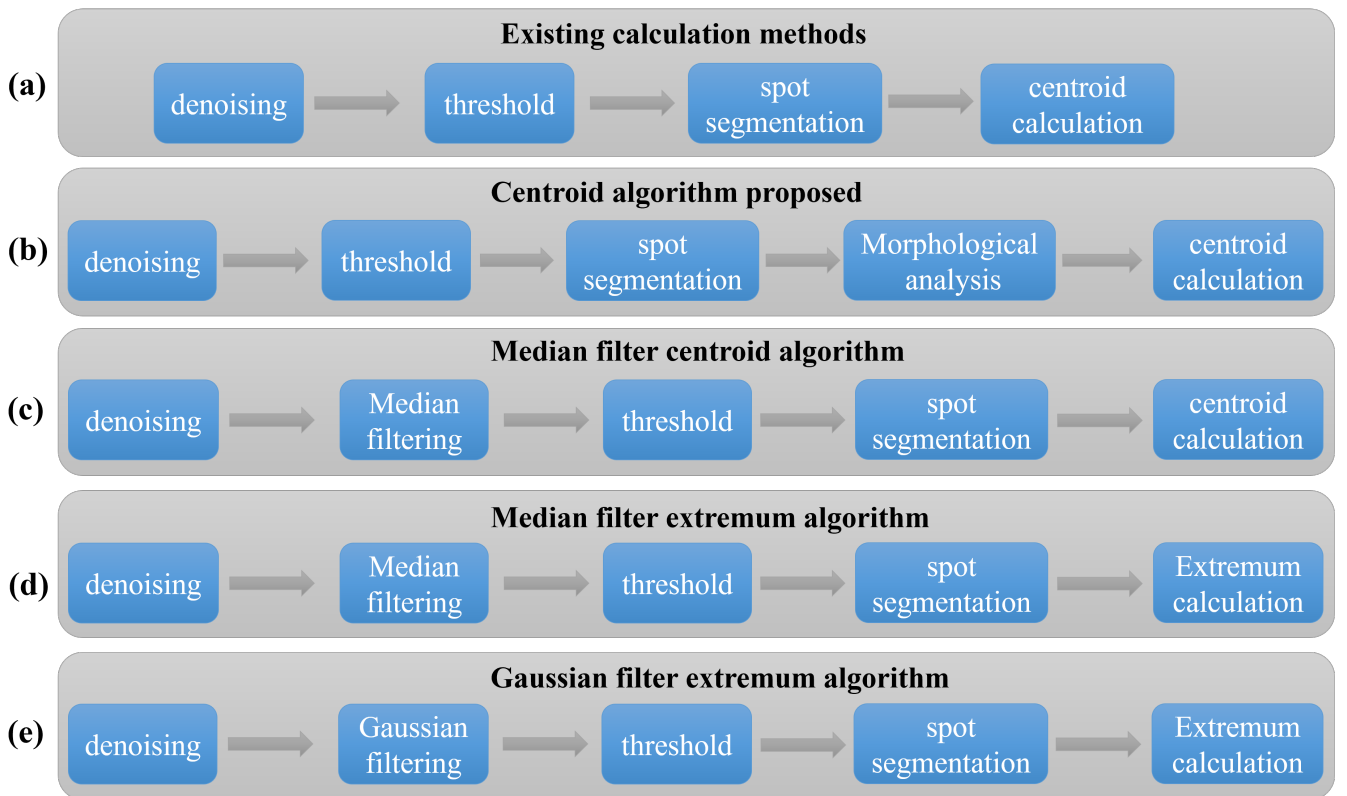


Fig. 4. (Color online) The process sketch of the reconstruction algorithm

The addition of median filtering and Gaussian filtering operations can solve two problems. For one thing, for the amount of data of "a large number of images \times hundreds of light spots", the faster algorithm obviously has more potential for development. Direct filtering calculation of the entire image is faster than analyzing the morphological characteristics of the light spots one by one. For another, in weak light detection such as neutron event imaging, noise elimination is an important task. Although weak noise with low gray values can be removed by thresholding, there are still many noises with large gray values but small areas (compared to signal gray and area) in weak light detection. It is difficult to remove these signal-like noises using centroid algorithm. However, the operation of filtering and threshold combination can eliminate noise with large gray value but small area, and better distinguish between noise and signal. Compared with median filtering, Gaussian filtering can reduce the gray value of noise to a greater extent and further enhance the signal-noise discrimination ability.

The addition of median filtering and Gaussian filtering operations can solve two problems. For one thing, for the amount of data of "a large number of images \times hundreds of light spots", the faster algorithm obviously has more potential for development. Direct filtering calculation of the entire image is faster than analyzing the morphological characteristics of the light spots one by one. For another, in weak light detection such as neutron event imaging, noise elimination is an important task. Although weak noise with low gray values can be removed by thresholding, there are still many noises with large gray values but small areas (compared to signal gray and area) in weak light detection. It is difficult to remove these signal-like noises using centroid algorithm. However, the operation of filtering and threshold combination can eliminate noise with large gray value but small area, and further enhance the signal-noise discrimination ability.

III. RESULTS AND DISCUSSION

A. Experimental Results and Evaluation

When the reactor power was near 10 MW, 1.9×10^5 images and 5×10^3 background images were collected, about 1.3 Tb. One of the original images is shown in Figure 5. The raw data contains light spots produced by neutron capture events, as well as a large amount of noise. The image noise obtained by CMOS sensor is mainly divided into random noise and fixed pattern noise.

Fixed pattern noise is mainly caused by reset voltage deviation. The reset voltage deviation is caused by factors such as the MOS FET threshold voltage deviation in the pixel, the gain deviation of the source follower, the gain and bias of the column amplifier, etc. This is a kind of non-transient spatial noise. Therefore, it can be eliminated by multi-frame averaging method. The average noise value of 5000 background images can be used to eliminate the fixed pattern noise to a certain extent.

There are many sources of random noise, such as power

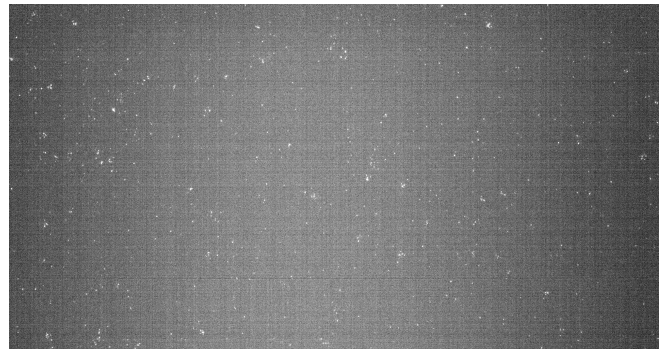


Fig. 5. Raw image data

voltage fluctuation, substrate coupling between CMOS sensor and peripheral devices, reset and readout process of pixel transistors. It mainly includes shot noise, dark current noise, transfer noise, reset noise, flicker noise ($1/f$), etc. The spatial distribution of random noise is not fixed, so it is not easy to remove it directly. It can be distinguished based on gray value and contour features in the reconstruction algorithm. For example, the morphological analysis link in the centroid algorithm (Figure 4b) is used to analyze the area, perimeter, shape and other characteristics of the light spot.

In order to compare the effects of neutron event imaging, traditional integral imaging results need to be obtained. By subtracting the multi-frame background average from the original image data, and then setting a threshold to remove the noise with low gray value noise, the integral imaging with 2 ms exposure was obtained. After superimposing 1.9×10^5 frames, the traditional integral imaging result is obtained, as shown in Figure 6. The Figure 6 shows that the $125 \mu\text{m}$ stripes of the resolution grating are clearly visible visually at a field of view of $2.7 \text{ cm} \times 2.7 \text{ cm}$. And it also shows four easily distinguishable peaks in the grayscale distribution map. For $100 \mu\text{m}$ stripes, it is difficult for the human eye to distinguish. And the gray distribution is not an ideal four peaks. Therefore, the resolution of the conventional method is considered to be at $125 \mu\text{m}$, and barely $100 \mu\text{m}$.

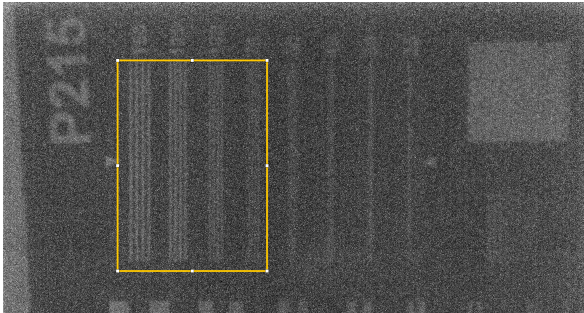
In the image reconstruction calculation, the centroid algorithm, median filter centroid algorithm, median filter extremum algorithm, and Gaussian filter extremum algorithm were used to calculate the occurrence position of neutron capture events in 1.9×10^5 images. High-resolution images were obtained. The results of the super-resolution experiment are shown in Figure 7. After analyzing, the spatial resolution of the super-resolution image is significantly improved and the results are shown in Table 1.

In order to more accurately evaluate the super-resolution effect of single neutron imaging, the image can be directly observed subjectively. In the objective aspect, the line pair gray analysis and modulation transfer function are used to evaluate the resolution improvement effect.

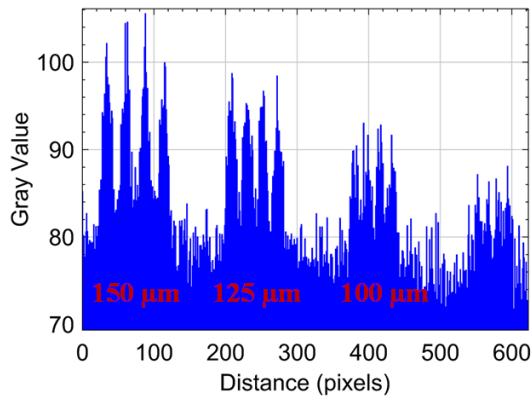
From the image results, the reconstruction results of the centroid algorithm in Figure 7(a)(b) can achieve a resolution of $50 \mu\text{m}$. In gray analysis, $50 \mu\text{m}$ stripes can be clearly distinguished, while $40 \mu\text{m}$ stripes cannot be distinguished.

Table 1. Super-resolution experimental results

	Traditional imaging (original image)	Single neutron imaging (super-resolution image)			
		Centroid algorithm	Median filtering centroid algorithm	Median filtering extremum algorithm	Gaussian filter extremum algorithm
Spatial resolution(μm)	100-125	50	40-50	40-50	40



(a) Neutron image.



(b) Grayscale distribution of ROI in sCMOS image.

Fig. 6. (Color online) Traditional integral imaging and its resolution level.

Median filtering centroid algorithm Figure 7(c)(d) and median filtering extremum algorithm Figure 7(e)(f) have similar effects. Both algorithms can achieve resolutions between $50\ \mu\text{m}$ and $40\ \mu\text{m}$. In grayscale analysis, $50\ \mu\text{m}$ stripes can be clearly distinguished, and $40\ \mu\text{m}$ stripes can be barely distinguished. The improvement in resolution shows that median filtering can eliminate more random noise. As the median filtering changes the signal distribution, it can further reduce the effect of noise on the neutron event discrimination. In addition, the extremum algorithm has a faster reconstruction speed (in this experiment, 5 times compared with centroid algorithm).

According to the reconstruction results Figure 7(g)(h), it can be considered that the gaussian filter extremum algorithm can achieve a resolution of $40\ \mu\text{m}$. The Gaussian Filter Extreme algorithm obtains the best resolution and the fastest reconstruction by virtue of its excellent random noise reduction and its ability to maintain the peaks constant.

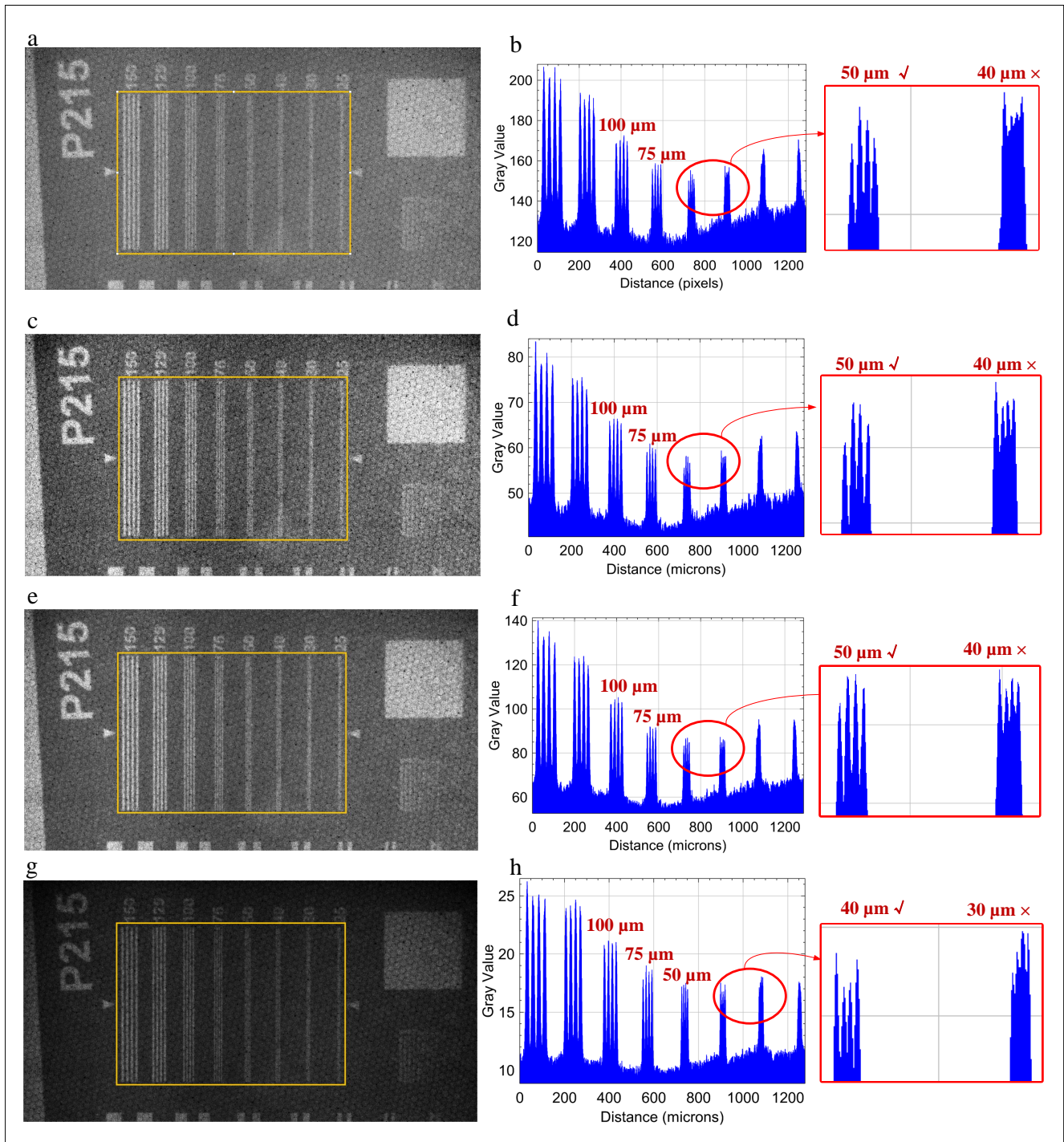


Fig. 7. (Color online) Super-resolution reconstruction results, and gray-scale distribution of resolution fringes.
 (a) Reconstruction results of centroid algorithm; (b) resolution fringes distribution calculated by centroid algorithm;
 (c) Reconstruction results of median filter centroid algorithm; (d) resolution fringes distribution calculated by median filter centroid algorithm;
 (e) Reconstruction results of median filter extremum algorithm; (f) resolution fringes distribution calculated by median filter extremum algorithm;
 (g) Reconstruction results of Gaussian filter extremum algorithm; (h) resolution fringes distribution calculated by Gaussian filter extremum algorithm.

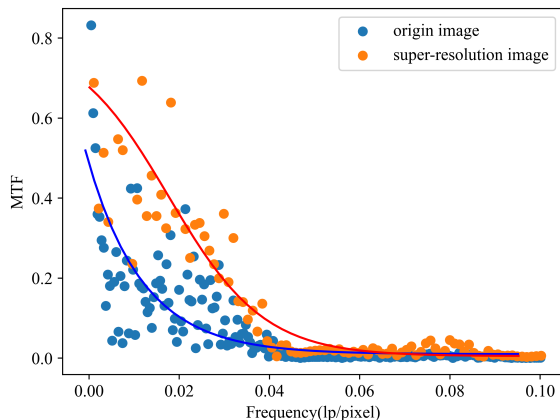


Fig. 8. (Color online)MTF curves of original image and super-resolution image

After comparing various algorithms, the results show that the Gaussian filter extreme value algorithm has the best effect. On the one hand, it is reflected in the resolution, where the algorithm is able to achieve an optimal level of resolution. On the other hand, it is reflected in the image quality, where the reconstructed image has higher clarity and better subjective visualization. In addition, it has the advantages of small calculation amount and high speed.

Modulation Transfer Function (MTF) is one of the important optical system evaluation indicators and can be used to calculate the resolution level. Although the method of observing line pairs is the most direct and reliable, MTF can still be used as an additional method to provide verification.

Computationally, the edge-to-edge method was chosen for the calculation of the MTF curve. In terms of calculation objects, due to the excellent performance of the Gaussian Filter Extreme algorithm, its reconstructed image is used as a representative of super-resolution. The MTF curves of the original and super-resolution images were compared, as shown in Figure 8. The resolution of the images calculated from the curves at 50 % and 10 % MTF is shown in Table 2.

At the same MTF, the super-resolution image has higher frequency line pairs, that is, the resolution level is also higher. The resolution obtained at 50 %MTF, the most sensitive human eye, is $41.7 \mu\text{m}$. The resolution obtained by directly observing the grayscale distribution of line pairs with the human eye is $40 \mu\text{m}$. Whether observing line pairs or analyzing MTF to assess resolution, the final results demonstrate that the experimental approach and reconstruction algorithm for single neutron imaging is an effective solution to greatly improve imaging resolution.

B. Algorithm feature mining

In order to more concretely demonstrate the functions and characteristics of the algorithm, a small area with a high

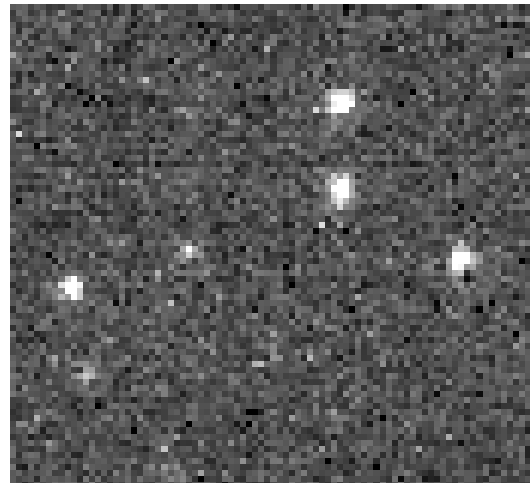


Fig. 9. (Color online)A small area of raw image data (86x80pixels).

signal-to-noise ratio was intercepted from the original image for independent calculation, as shown in Figure 9.

The specific calculation steps and processing effects of the centroid algorithm are shown in Figure 10. (I) Most of the random noise in Figure 10(a) can be removed by setting threshold segmentation spots. According to Figure 10(b), it can be found that there are still many noises with higher gray value. In order to minimize the loss of neutron signal, the threshold cannot be further increased to remove noise. (II) Contour feature discrimination is a feasible method for further processing. The contour features were calculated using Suzuki85 boundary tracking algorithm as shown in Figure 10(c). (III) Neutron signals can be filtered out based on the contour features. Finally, the distribution of pixel positions where the neutron signals are located were reconstructed as in Figure 10(d).

The characteristic of the centroid algorithm is that it can analyze light spot one by one, and perform processing based on the shape, area, perimeter and other image moment information. The centroid algorithm has many adjustable parameters, mainly including threshold parameters and spot image moment parameters. However, the disadvantage is that the effect of noise elimination is not good and the calculation amount is large.

The Gaussian filter algorithm can improve the resolution from $125 \mu\text{m}$ to $40 \mu\text{m}$. In order to more concretely demonstrate the functions and characteristics of the algorithm, the intermediate calculation results are given in Figure 11. (I) Through Gaussian filtering, the random noise in Figure 11(a) were reduced and smoothed, and the result of Figure 11(b) was obtained. The distribution area of light spots with low SNR and random noise is generally smaller. Gaussian filtering can greatly reduce their gray scale, so that they can be better filtered. (II)Therefore, setting a lower threshold after Gaussian filtering can effectively segment out the signal spots, as shown in Figure 11(c). (III) Finally, the single-pixel distribution of the neutron signal was reconstructed, as shown in Figure 11(d).

Table 2. Resolution size under different discrimination conditions

Data	Grayscale analysis of line pairs	50 % MTF	10 % MTF
Origin Image	125 μm	375.1 μm	21.2 μm
Super-Resolution Images	40 μm	41.7 μm	12 μm

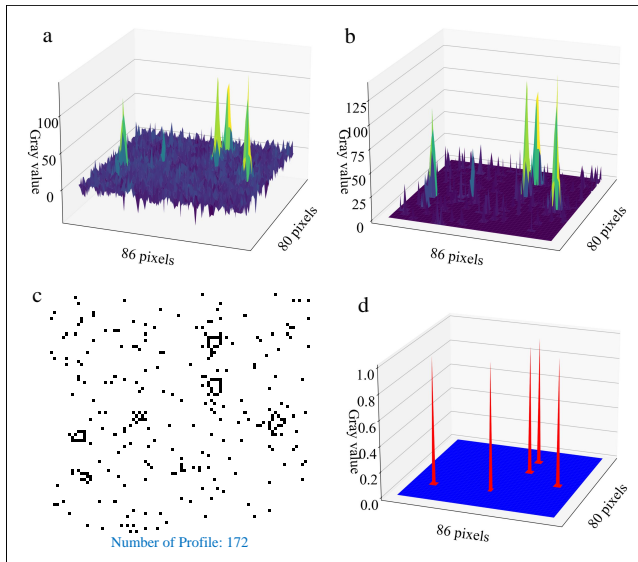


Fig. 10. (Color online)Centroid algorithm :
(a) Grayscale distribution of original data; (b) Grayscale distribution after spot segmentation; (c) Contour line of light spot; (d) Grayscale distribution of reconstruction results.

Gaussian filtering algorithms not only have a stronger signal-to-noise screening capability, but also possess a faster speed. In addition, the algorithm can flexibly adjust the array size of the Gaussian filter kernel, the sigma value, and the spot segmentation threshold. These variable parameters enable the algorithm to remain well adapted under different experimental conditions, ensuring effective screening of neutron signals and noise.

IV. CONCLUSION

This work proved the principle of super-resolution imaging based on neutron capture events. A super-resolution imaging instrument was installed on the cold neutron source of the CMRR. The commonly used $^6\text{LiF-ZnS}$ scintillation screen, MCP and CMOS were used in the hardware. The weak light signal produced by neutron capture event was successfully detected, and super-resolution imaging was achieved using a reconstruction algorithm.

For one thing, super-resolution imaging based on neutron capture events requires processing a large amount of image data, so computing time is an important factor. The median filtering extremum algorithm and Gaussian filtering ex-

tremum algorithm proposed in this work can process pixel clusters frame by frame rather than one by one. The reconstruction speed of these two methods is faster. For another, it

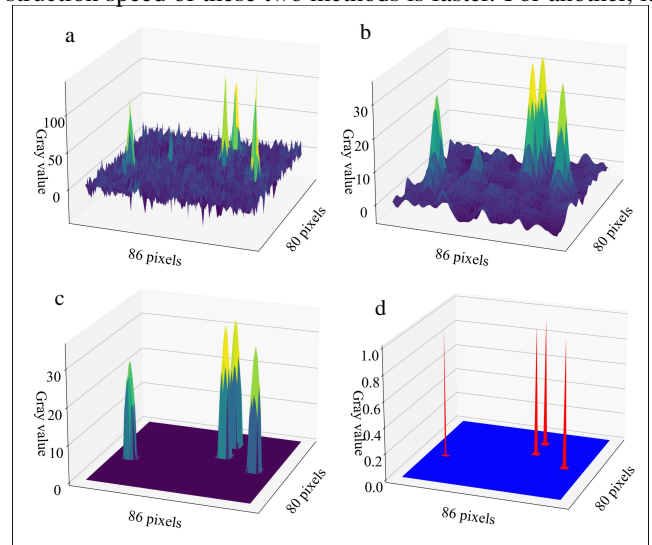


Fig. 11. (Color online)Gaussian filter algorithm:
(a) Grayscale distribution of original data; (b) Grayscale distribution after filtering; (c) Grayscale distribution after spot segmentation; (d) Grayscale distribution of reconstruction results.

is crucial to deal with the noise generated by MCP and CMOS in super-resolution imaging. The Gaussian filter extremum algorithm can effectively distinguish signals and noise, reduce signal loss, and do not change the peak position of the light spot. In this experiment, the resolution can be improved from 125 μm to 40 μm , with an improvement of 68 %.

This work provides solutions both experimentally and computationally, and proves that these solutions have better performance in methodology. If better resolution is pursued, it can be achieved with a smaller field of view, a thinner $\text{Gd}_2\text{O}_2\text{S}$ scintillation screen, and a smaller MCP aperture. Neutron super-resolution imaging can significantly improve spatial resolution, which is more attractive for many studies with non-destructive testing requirements. Non-destructive high-resolution testing will also promote more research and application.

V. REFERENCE

- [1] R. He, X.Y. Niu, Y. Wang, et al., Advances in nuclear detection and readout techniques, *Nuclear Science and Techniques*, 34, 205 (2023). <https://doi.org/10.1007/s41365-023-01359-0>
- [2] J. Dumazert, R. Coulon, Q. Lecomte, et al., Gadolinium for neutron detection in current nuclear instrumentation research: A review, *Nuclear Instruments and Methods in Physics Research Section A: Accelerators, Spectrometers, Detectors and Associated Equipment*, 882, 53-68 (2018). <https://doi.org/10.1016/j.nima.2017.11.032>
- [3] E. Lehmann, Status and Progress in Neutron Imaging Detection Systems, IAEA-TECDOC. Vienna: IAEA, 261-271 (2020). <https://inis.iaea.org/search/search.aspx?orig-q=RN:52019820>
- [4] L.F. He, S.B. Han, G.H. Wei, et al., Development and Application of Neutron Imaging Technique at China Advanced Research Reactor, *Materials Science Forum*, 850, 153-160 (2016). <https://doi.org/10.4028/www.scientific.net/MSF.850.153>
- [5] D.K. Aswal, P.S. Sarkar, Y.S. Kashyap, *Neutron Imaging: Basics, Techniques and Applications*, Springer, 2022. <https://doi.org/10.1007/978-981-16-6273-7>
- [6] N. Kardjilov, I. Manke, R. Woracek, et al., Advances in neutron imaging, *Materials Today*, 21, 652-672 (2018). <https://doi.org/10.1016/j.mattod.2018.03.001>
- [7] J. Disch, L. Bohn, S. Koch, et al., High-resolution neutron imaging of salt precipitation and water transport in zero-gap CO₂ electrolysis, *Nature Communications*, 13, 6099 (2022). <https://doi.org/10.1038/s41467-022-33694-y>
- [8] N. Kardjilov, I. Manke, M. Strobl, et al., Three-dimensional imaging of magnetic fields with polarized neutrons, *Nature Physics*, 4, 399-403 (2008). <https://doi.org/10.1038/nphys912>
- [9] M. Strobl, C. Grünzweig, A. Hilger, et al., Neutron dark-field tomography, *Physical review letters*, 101, 123902 (2008). <https://doi.org/10.1103/PhysRevLett.101.123902>
- [10] R. Woracek, D. Penmadu, N. Kardjilov, et al., 3D Mapping of Crystallographic Phase Distribution using Energy-Selective Neutron Tomography, *Advanced Materials*, 26, 4069-4073 (2014). <https://doi.org/10.1002/adma.201400192>
- [11] R. Woracek, M. Krzyzagorski, H. Markötter, et al., Spatially resolved time-of-flight neutron imaging using a scintillator CMOS-camera detector with kHz time resolution, *Opt. Express*, 27, 26218-26228 (2019). <https://doi.org/10.1364/OE.27.026218>
- [12] R.F. Ziesche, N. Kardjilov, W. Kockelmann, et al., Neutron imaging of lithium batteries, *Joule*, 6, 35-52 (2022). <https://doi.org/10.1016/j.joule.2021.12.007>
- [13] X. Yuan, S.S. Han, Single-pixel neutron imaging with artificial intelligence: Breaking the barrier in multi-parameter imaging, sensitivity, and spatial resolution, *The Innovation*, 2, (2021). <https://doi.org/10.1016/j.xinn.2021.100100>
- [14] S. Wang, C. Cao, W. Yin, et al., A novel NDT scanning system based on line array fast neutron detector and DT neutron source, *Materials*, 15, 4946 (2022). <https://doi.org/10.3390/ma15144946>
- [15] A. Tengattini, N. Kardjilov, L. Helfen, et al., Compact and versatile neutron imaging detector with sub-4 micrometer spatial resolution based on a single-crystal thin-film scintillator, *Opt. Express*, 30, 14461-14477 (2022). <https://doi.org/10.1364/OE.448932>
- [16] Y.S. Song, J. Conner, X.D. Zhang, et al., Monte Carlo simulation of a very high resolution thermal neutron detector composed of glass scintillator microfibers, *Applied Radiation and Isotopes*, 108, 100-107 (2016). <https://doi.org/10.1016/j.apradiso.2015.12.035>
- [17] H.Z. Bilheux, R. McGreevy, I.S. Anderson, *Neutron Imaging and Applications: A Reference for the Imaging Community*, Springer, 2009. <https://doi.org/10.1007/978-0-387-78693-3>
- [18] E.H. Lehmann, D. Mannes, M. Strobl, et al., Improvement in the spatial resolution for imaging with fast neutrons, *Nuclear Instruments and Methods in Physics Research Section A: Accelerators, Spectrometers, Detectors and Associated Equipment*, 988, 164809 (2021). <https://doi.org/10.1016/j.nima.2020.164809>
- [19] P. Trtik, J. Hovind, C. Grünzweig, et al., Improving the Spatial Resolution of Neutron Imaging at Paul Scherrer Institut – The Neutron Microscope Project, *Physics Procedia*, 69, 169-176 (2015). <https://doi.org/10.1016/j.phpro.2015.07.024>
- [20] D.Y. Li, S. Wang, H.Y. Huo, et al., Design Optimization and Characterization of Cold Neutron Imaging Detector Based on Novel Gadolinium Scintillation Glass Fiber Arrays and Infinity Corrected Optics, *IEEE Transactions on Nuclear Science*, 69, 2162-2167 (2022). <https://doi.org/10.1109/TNS.2022.3208234>
- [21] H.Y. Huo, H. Li, Y. Wu, et al., Development of Cold Neutron Radiography Facility (CNRF) based on China Mianyang Research Reactor (CMRR), *Nuclear Instruments and Methods in Physics Research Section A: Accelerators, Spectrometers, Detectors and Associated Equipment*, 953, 163063 (2020). <https://doi.org/10.1016/j.nima.2019.163063>
- [22] E.H. Lehmann, *Basics of Neutron Imaging*, (2023). <https://doi.org/10.5772/intechopen.110403>
- [23] W. Wang, Q.H. Wang, Q. Yang, et al., Experimental study of spatial resolution of MCPs for compact high-resolution neutron radiography system, *Nuclear Instruments and Methods in Physics Research Section A: Accelerators, Spectrometers, Detectors and Associated Equipment*, 1050, 168179 (2023). <https://doi.org/10.1016/j.nima.2023.168179>
- [24] S. Han, M. Wu, H. Wang, et al., Design of cold neutron imaging facility at China advanced research reactor, *Physics Procedia*, 43, 73-78 (2013). <https://doi.org/10.1016/j.phpro.2013.03.009>
- [25] H. Li, S. Wang, C. Cao, et al., Neutron imaging development at China academy of engineering physics (CAEP), *Physics Procedia*, 88, 154-161 (2017). <https://doi.org/10.1016/j.phpro.2017.06.021>
- [26] Z.H. Wang, C. Dujardin, M.S. Freeman, et al., Needs, trends, and advances in scintillators for radiographic imaging and tomography, *IEEE Transactions on Nuclear Science*, (2023). <https://doi.org/10.1109/TNS.2023.3290826>
- [27] L.X. Zhang, S.Z. Chen, Z.D. Zhang, et al., Resolution analysis of thermal neutron radiography based on accelerator-driven compact neutron source, *Nuclear Science and Techniques*, 34, 76 (2023). <https://doi.org/10.1007/s41365-023-01227-x>
- [28] N. Kalyvas, P. Liaparinos, Analytical and Monte Carlo comparisons on the optical transport mechanisms of powder phosphors, *Optical Materials*, 88, 396-405 (2019). <https://doi.org/10.1016/j.optmat.2018.12.006>
- [29] X.F. Jiang, Q.L. Xiu, J.R. Zhou, et al., Study on the neutron imaging detector with high spatial resolution at China spallation neutron source, *Nuclear Engineering and Technology*, 53, 1942-1946 (2021). <https://doi.org/10.1016/j.net.2020.12.009>
- [30] B. Winkler, Applications of neutron radiography and neutron tomography, *Reviews in Mineralogy and Geochemistry*, 63,

- 459-471 (2006). <https://doi.org/10.2138/rmg.2006.63.17>
- [31] Y.H. He, Y.Y. Huang, Z.R. Zeng, et al., Single-pixel imaging with neutrons, *Science Bulletin*, 66, 133-138 (2021). <https://doi.org/10.1016/j.scib.2020.09.030>
- [32] J.Y. Tang, Q. An, J.B. Bai, et al., Back-n white neutron source at CSNS and its applications, *Nuclear Science and Techniques*, 32, 1-10 (2021). <https://doi.org/10.1007/s41365-021-00846-6>
- [33] J.X. Zheng, Y. Zeng, J.J. Wang, et al., Hydrogen-rich 2D halide perovskite scintillators for fast neutron radiography, *Journal of the American Chemical Society*, 143, 21302-21311 (2021). <https://doi.org/10.1021/jacs.1c08923>
- [34] S.X. Wang, S.H. Deng, Z.J. Tan, et al., The multifunctional neutron imaging system at GPPD: Design, principles and applications, *Nuclear Instruments and Methods in Physics Research Section A: Accelerators, Spectrometers, Detectors and Associated Equipment*, 1052, 168315 (2023). <https://doi.org/10.1016/j.nima.2023.168315>
- [35] S. Koerner, E. Lehmann, P. Vontobel, Design and optimization of a CCD-neutron radiography detector, *Nuclear Instruments and Methods in Physics Research Section A: Accelerators, Spectrometers, Detectors and Associated Equipment*, 454, 158-164 (2000). [https://doi.org/10.1016/S0168-9002\(00\)00819-6](https://doi.org/10.1016/S0168-9002(00)00819-6)
- [36] I. Mor, N. Eldad, M. Cohen, et al., Development of a CCD based thermal neutron imaging detector for the Israeli Research Reactor IRR-1 at Soreq NRC, *Nuclear Instruments and Methods in Physics Research Section A: Accelerators, Spectrometers, Detectors and Associated Equipment*, 1012, 165632 (2021). <https://doi.org/10.1016/j.nima.2021.165632>
- [37] Y. Liu, T.F. Zhu, Z. Luo, et al., First-order primal-dual algorithm for sparse-view neutron computed tomography-based three-dimensional image reconstruction, *Nuclear Science and Techniques*, 34, 118 (2023). <https://doi.org/10.1007/s41365-023-01258-4>
- [38] B. Tang, W. Yin, Q. Wang, et al., High Quantum Efficiency Rare-Earth-Doped Gd₂O₂S: Tb, F Scintillators for Cold Neutron Imaging, *Molecules*, 28, 1815 (2023). <https://doi.org/10.3390/molecules28041815>
- [39] L. Chen, Z. Bai, Q. Liu, Photoluminescence/cathodoluminescence properties and energy transfer mechanisms of fine-particle Gd₂O₂S:Tb³⁺, RE³⁺ (RE = Dy, Eu) phosphor, *Journal of Luminescence*, 267, 120343 (2024). <https://doi.org/10.1016/j.jlumin.2023.120343>
- [40] O.H. Siegmund, J.V. Vallerger, A.S. Tremsin, et al., High spatial resolution neutron sensing microchannel plate detectors, *Nuclear Instruments and Methods in Physics Research Section A: Accelerators, Spectrometers, Detectors and Associated Equipment*, 576, 178-182 (2007). <https://doi.org/10.1016/j.nima.2007.01.148>
- [41] Y.H. Ma, H. Li, X. Yang, et al., Wide energy region efficiency calibration study of a prompt gamma activation analysis facility, *Journal of Radioanalytical and Nuclear Chemistry*, 1-10 (2023). <https://doi.org/10.1007/s10967-023-09097-8>
- [42] Y.H. Ma, X. Yang, H.Y. Huo, et al., Measurement study of neutron field relative distribution in sample for PG-NAA based on NT, *Nuclear Instruments and Methods in Physics Research Section A: Accelerators, Spectrometers, Detectors and Associated Equipment*, 1045, 167451 (2023). <https://doi.org/10.1016/j.nima.2022.167451>